Characterization of $BaZrO_3$ Nanoparticles Prepared by Reverse Micelle Synthesis

Keith J. Leonard,*,† Srivatsan Sathyamurthy,‡ and M. Parans Paranthaman‡

Metals and Ceramics Division and Chemical Sciences Division, Oak Ridge National Laboratory, Oak Ridge, Tennessee 37831

Received March 24, 2005. Revised Manuscript Received June 2, 2005

Nanoparticles of $BaZrO_3$ have been prepared through a reverse micelle synthesis. The as-processed particles consisted of amorphous Ba−Zr−O and crystalline $Zr_{0.95}O_2$ particles with an average diameter of approximately 7.5 nm. Conversion of the powders to crystalline $BaZrO_3$ nanoparticles occurred upon heat treatment at 700 °C in air for 0.5 h. The heat-treated powder consisted primarily of $BaZrO_3$ and a small quantity of ZrO_2, with an average particle size increase to 17.3 nm. The as-processed and heat treated nanoparticles were analyzed by both X-ray diffraction and transmission electron microscopy. The nanocrystalline $BaZrO_3$ particles were characterized as having a faceted octahedral shape with {100} and {111} surfaces. A brief evaluation of the stability of these surfaces is also discussed.

Introduction

Research into nanotechnology has exploded over the past several years carrying with it new ideas in both processing and utilization of nanostructured materials for a magnitude of applications ranging from common uses to advanced technologies over all scientific and commercial fields. Numerous preparation methods for nanoscaled materials, particularly particles, have been established and documented. These processes include physical methods such as mechanical milling[1] and inert gas condensation,[2] along with chemical methods such as oxidative precipitation,[3] electrodeposition,[4] hydrothermal[5−6] and sol−gel synthesis.[7−10] In general, a major benefit of chemical methods is their relatively inexpensive investment of capital equipment. Of these chemical processes, reverse micelle synthesis has been recently demonstrated to be a viable method for producing a wide array of metals and metal oxide compounds including perovskites[11−16] over a relatively narrow particle size distribution.

Reverse micelle synthesis utilizes the natural phenomenon involving the formation of spheroidal aggregates in a solution when a surfactant is introduced to a polar organic solvent, formed either in the presence or in the absence of water.[11] Micelle formation allows for a unique encapsulated volume of controllable size through which reactions and subsequent development of metal and metallic compounds can be produced. Aggregates containing water to surfactant molar ratios of less than 15 are called reverse micelles and have hydrodynamic diameters in the range of 4−10 nm,[11,13−14,17] whereas water to surfactant molar ratios of greater than 15 constitute microemulsions, which have a hydrodynamic diameter range between 5 and 500 nm. Within the micelles, reactants for chemical processes can be contained. In developing nanocrystalline materials, solutions of separately prepared reverse micelles containing encapsulate reactants A and B are mixed together. By using sonication or stirring to further enhance collisions between the micelles containing the different reactants, fusion between two micelles can occur, which produces a transient dimer that exchanges the water cores of the collided micelles. The dimer breaks down again into two reverse micelles with the contents from one micelle transferred into the other.[11] The mixing of the two reactants produces a precipitation reaction, from which nanoparticles can be obtained through centrifugal extraction of the solution. The process of micelle exchange, which leads to further growth, continues until the particles reach a terminal size determined by the system and the stabilization of the particles by the surfactant.[14] The size of the metallic particles produced is a function of the reaction time, water

* Corresponding author. Phone: (865)576-3687; e-mail: leonardk@ornl.gov.
† Metals and Ceramics Division.
‡ Chemical Sciences Division.

(1) Gotic, M.; Czako-Nagy, I.; Popovic, S.; Music, S. *Philos. Mag. Lett.* **1998**, *78*, 193.
(2) Schaefer, J. E.; Kisker, H.; Kronmüller, H.; Würschum, R. *Nanostructured Mater.* **1992**, *1*, 6, 523.
(3) Sartale, S. D.; Lokhande, C. D. *Indian J. Eng. Mater. Sci.* **2000**, *7*, 404.
(4) Erb, U. *Nanostructured Mater.* **1995**, *6*, 5−8, 533.
(5) Komarneni, S.; D'Arrigo, M. C.; Leionelli, C.; Pellacani, G. C.; Katsuki, H. *J. Am. Ceram. Soc.* **1998**, *81*, 3041.
(6) Athawale, A. A.; Bapat, M. *J. Metastable Nanocrystalline Mater.* **2005**, *23*, 3.
(7) Boschini, F.; Guillaume, B.; Rulmont, A.; Cloots, R. *Key Eng. Mater.* **2004**, *264−268*, 2335.
(8) Phulé, P. P.; Grundy, D. C. *Mater. Sci. Eng.* **1994**, *B23*, 29.
(9) Veith, M.; Mathur, S.; Lecerf, N.; Huch, V.; Decker, T.; Beck, H. P.; Eiser, W.; Haberkorn, R. *J. Sol−Gel Sci. Technol.* **2000**, *15*, 145.
(10) Chatterjee, A.; Das, D.; Pradhan, S. K.; Chakravorty, D. *J. Magn. Magn. Mater.* **1993**, *127*, 1−2, 214.
(11) Misra, R. D. K.; Gubbala, S.; Kale, A.; Egelhoff, W. F., Jr. *Mater. Sci. Eng.* **2004**, *B111*, 164.
(12) Sugimoto, T.; Kimijima, K. *J. Phys. Chem. B* **2003**, *107*, 10753.
(13) Dixit, S. G.; Mahadeshwar, A. R.; Haram, S. K. *Colloids Surf., A* **1998**, *133*, 69.
(14) McLeod, M. C.; McHenry, R. S.; Beckman, E. J.; Roberts, C. B. *J. Phys. Chem. B* **2003**, *107*, 2693.
(15) Sun, W.; Xu, L.; Chu, Y.; Shi, W. *J. Colloid Interface Sci.* **2003**, *266*, 99.
(16) Yuasa, M.; Sakai, G.; Shimanoe, K.; Teraoka, Y.; Yamazoe, N. *J. Electrochem. Soc.* **2004**, *151*, 9, A1477.
(17) Fendler, J. H. *Chem. Rev.* **1987**, *87*, 877.

10.1021/cm0506454 CCC: $30.25
Published on Web 07/01/2005

content in the micelle, the concentration of reactant solutions contained within the micelle, and the solvent type.[14]

Metal oxide compounds of the perovskite crystal structure are a class of materials that have attracted great attention for their use in the electronics industry due to unique optical, magnetic, and electronic properties.[18] These properties, which have been found to be dependent on the dimensional scale of the materials, are the driving force into research examining these compounds in particle[19,20] or thin-film forms.[21] Recently, a dispersion of $BaZrO_3$ nanoparticles in laser ablated $YBa_2Cu_3O_{7-\delta}$ (YBCO) films has been produced through the initial mixing, compacting, and sintering of YBCO with $Ba(NO_3)_2$ and ZrO_2 powders in the ablation targets,[22] producing stable flux-pinning centers around the $BaZrO_3$ nanoparticles within the superconducting film. Alhough not restricted to $BaZrO_3$ alone, the use of dopant particles in YBCO films for flux pinning enables the conduction of large supercurrents under the presence of magnetic fields.[23] Dramatic enhancements to the critical currents by a factor of 1.5 to 5 have been observed for these films under magnetic fields.[22] This method also offers an easier processing route than heavy-ion irradiation in producing defect generated pinning centers, in addition to being more amenable to the production of long-length multilayered coated conductor tapes.[22] Furthermore, recent work at Oak Ridge has shown that pulsed laser deposition of $BaZrO_3$-doped YBCO targets results in an even finer dispersion of $BaZrO_3$ particles within the YBCO film.

Synthesis of $BaZrO_3$ particles through solution-based techniques have been reported with particles ranging from micron[20] to nanocrystalline[6−9] sizes. In the latter, sol-precipitation and hydrothermal synthesis was successful in producing amorphous nanoparticles, which upon heat treatment developed into either micron-sized particles[6−8] or nanocrystalline agglomerations of micron scale particles.[9] For the use of $BaZrO_3$ particles as flux-pinning centers, larger particle sizes may create nonuniform distributions or larger particle sizes if used within ablation or sputtering targets. In this paper, we report on the processing of $BaZrO_3$ nanoparticles produced through reverse micelle synthesis. Emphasis is placed on characterizing two of the processing stages in production through X-ray diffraction and analytical electron microscopy.

Experimental Procedures

All chemicals were used as received. Barium nitrate ($Ba(NO_3)_2$, Alfa Aesar: 99+%) and zirconium dinitrate oxide ($ZrO(NO_3)_2 \times H_2O$, Alfa Aesar: 99.9%) were used as the starting materials for the barium zirconate nanoparticles, and sodium hydroxide (Fisher Scientific 97.7%) was used as the precipitating agent. The microemulsion system used in the study consisted of *n*-octane (Alfa Aesar: 99%) as the continuous oil phase, cetyl trimethylammonium bromide (CTAB) (Alfa Aesar: 99%) as the surfactant, 1-butanol (Alfa Aesar: 99.4%) as the cosurfactant, and an aqueous solution as the dispersed phase. A solution containing 0.12 M Ba^{2+} and Zr^{4+} was prepared by dissolving 0.627 g of $Ba(NO_3)_2$ and 0.555 g of $ZrO(NO_3)_2 \times H_2O$ in 20 mL of deionized water. This solution was dispersed in a mixture of 28 g of *n*-octane, 6 g of 1-butanol, and 8 g of CTAB to form a microemulsion. Another microemulsion of similar composition using 20 mL of 0.72 M $(OH)^-$ solution (0.576 g of NaOH in 20 mL of deionized water) was prepared. The two microemulsions were mixed together using a magnetic stirrer for 1 h. The white precipitate that formed was extracted by centrifuging at 10 000 rpm for 10 min. The precipitate was then washed with methanol and dried in an oven at 110 °C. After grinding, the dried powders were heat-treated in separate batches for 30 min in stagnant air at temperatures increasing every 100 °C from 100 to 700 °C.

Characterization of the powders was performed through X-ray diffraction (XRD) in both the as-processed and heat-treated conditions. Samples for TEM were prepared from the as-processed and 700 °C treated particles. For TEM, the particles were suspended in a solution of methanol and mixed in a sonicator for approximately 5 min prior to sampling. Type-A lacey carbon films purchased from Ted Pella, Inc. were used to support the particles for electron microscopy. Prior to sampling, the Formvar backing of the lacey carbon film was removed by dipping the vertically oriented TEM grid in and out of chloroform for approximately 20 s. After air-drying, the TEM grids were dipped 4 times in and out of the sonicated particle suspensions. Extra care was taken in cleaning all glassware and tweezers used so as not to introduce foreign particles or to cross-contaminate.

The as-processed and postheat-treated samples were examined using a Philips CM200 TEM operated at 200 kV in both conventional and nanoprobe modes. Energy dispersive spectroscopy (EDS) was also carried out on the particles. The distribution and agglomeration of the particles on the lacey carbon films was found to be adequate for analysis.

Results and Discussion

The XRD $\theta-2\theta$ scan for the as-processed sample, Figure 1, revealed a predominately amorphous structure for the particles. However, some peaks were determined to be associated with the $Ba(OH)_2(H_2O)_3$ and $Zr_{0.95}O_2$ phases, although these were not positively identified until TEM analysis was conducted. Heat-treatment of the batches of as-processed powders in air for 0.5 h revealed no development of crystallinity for temperatures below 700 °C. For comparison, the XRD scan of the crystallized powders from the 700 °C treatment is shown with that of the as-processed powders in Figure 1. Clearly defined peaks of $BaZrO_3$ are observed within the $\theta-2\theta$ scan, along with minor peaks associated with the ZrO_2 phase. The crystallization of the nanoparticles at 700 °C in this study is 100 °C higher than the reported crystallization temperature for sol−gel processed $BaZrO_3$ particles.[8,9] In both as-processed and heat-treated samples, the zirconium oxide particles were determined to be tetragonal. This coincided with previous reports as to the tetragonal structure being stable at particle sizes below the range of 30 nm with larger particle sizes favoring the monoclinic structure.[24−26]

Examination of the as-processed particles through TEM confirmed the amorphous structure of the particles as

(18) Urban, J. J.; Yun, W. S.; Gu, Q.; Park, H. J. *Am. Chem. Soc*. **2002**, *124*, 7, 1186.
(19) Sin, A.; El Montaser, B.; Odier, P.; Weiss, F. *J. Am. Ceram. Soc*. **2002**, *85*, 8, 1928.
(20) Lu, Z.; Tang, Y.; Chen, L.; Li, Y. *J. Cryst. Growth* **2004**, *266*, 539.
(21) Paranthaman, M.; Shoup, S. S.; Beach, D. B.; Williams, R. K.; Specht, E. D. *Mater. Res. Bull.* **1997**, *32*, 12, 1697.
(22) Macmanus-Driscoll, J. L.; Foltyn, S. R.; Jia, Q. X.; Wang, H.; Serquis, A.; Civale, L.; Maiorov, B.; Hawley, M. E.; Maley, M. P.; Peterson, D. E. *Nature* **2004**, *3*, 439.
(23) Christen, D. *Nature* **2004**, *3*, 421.

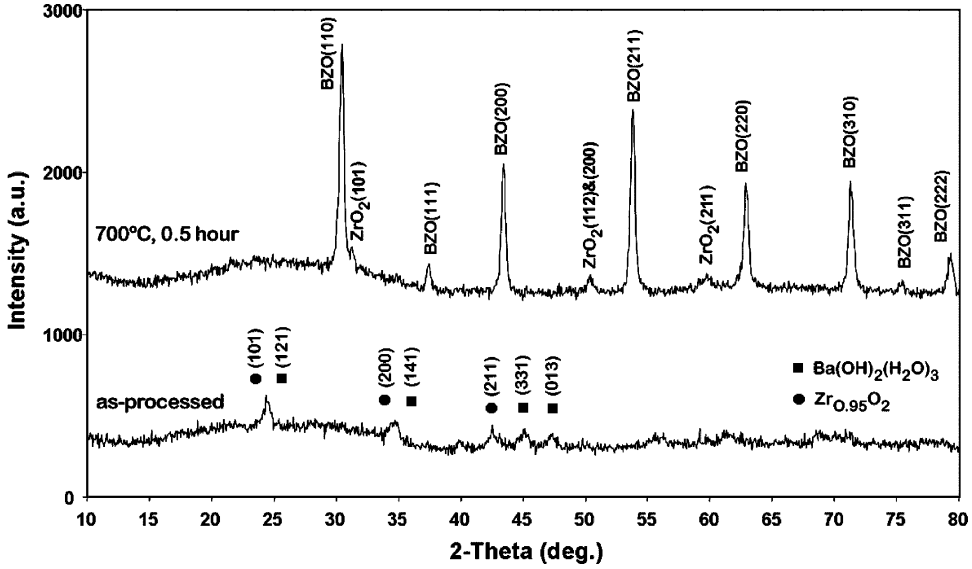

Figure 1. Comparison of X-ray diffraction scans for the as-processed and 700 °C heat-treated samples showing the development of $BaZrO_3$ (BZO). In addition to the $BaZrO_3$ phase, a small quantity of the ZrO_2 phase was also observed. The X-ray intensity for the heat-treated sample has been shifted upward for clarity.

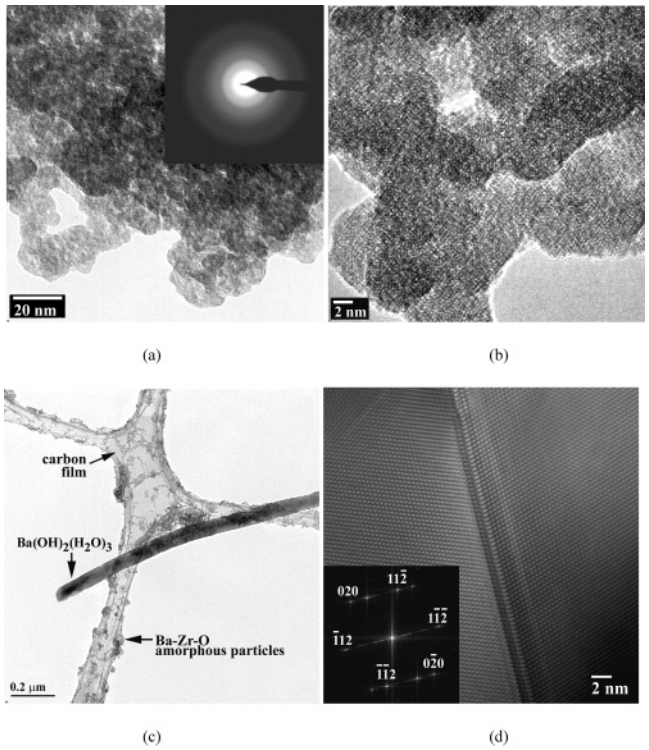

Figure 2. TEM micrographs of the as-processed Ba−Zr−O sample. (a) Low and (b) high magnification images of the amorphous particles with insert showing the amorphous SAD pattern. (c) Low magnification image showing $Ba(OH)_2(H_2O)_3$ rodlike particles caught on the lacey carbon grid. (d) Lattice image, $b = [201]$, of a {112} twinned interface contained within the BaO_2 particles following beam induced transformation from the $Ba(OH)_2(H_2O)_3$ phase by the microscope. Insert shows the fast Fourier transformation of the lattice image illustrating the twin.

indicated by XRD analysis. Figure 2a is a low magnification image of a particle agglomeration with the insert showing the amorphous pattern of the selected area diffraction (SAD) image taken of the particles. The particles were found to be more easily identifiable when agglomerated in groups suspended over the edge of a hole on the carbon film rather than as individual particles spread out over the carbon film due to the lack of contrast associated with their amorphous structure. The amorphous structure of the particles is also evident in the higher magnification image of Figure 2b.

The average diameter of the amorphous Ba−Zr−O particles, measured from several TEM micrographs at high magnification, was found to be approximately 7.5 nm with a spread of ±2 nm. The lack of contrast associated with the amorphous particles made it too difficult to obtain a statistically accurate particle size distribution. However, the particles observed were within the 4−10 nm hydrodynamic diameter range for reverse micelle structures.[13,17] The investigation of multiple particle agglomerations collected on the sample grid at different areas was unsuccessful in identifying any crystalline $Zr_{0.95}O_2$ particles as detected by XRD analysis. An EDS spectrum taken from an agglomeration of the as-processed particles is shown in Figure 3a. The presence of Cu within the spectrum arises from the mesh grid supporting the lacey carbon film. In addition, levels of K, Ca, and Br were also detected within the particle agglomeration from the process solution producing the nanoparticles. The level of Ba detected in the EDS spectrum of the as-processed material appeared to be slightly depleted in comparison to the spectrum taken from a $BaZrO_3$ particle of the postheat-treated sample (Figure 3b, to be discussed later). This was likely due to the presence of the $Zr_{0.95}O_2$ particles within the agglomeration analyzed. In addition to the nanoparticles, Ba-rich rodlike structures were observed in the as-processed sample, further skewing the nominal composition of the measured agglomeration toward that of Ba deficient.

The rodlike particles (Figure 2c) identified though EDS as a barium-oxide were consistent in size with average diameters of 62 nm and lengths of 1.5 μm, although some particles were broken in two. The rods typically had a

(24) Woudenberg, F. C. M.; Sager, W. F. C.; Sibelt, N. G. M.; Verweij, H. *Adv. Mater.* **2001**, *13*, 7, 514.
(25) Shankar, S. S.; Joshi, H.; Pasricha, R.; Pavaskar, N. R.; Mandale, A. B.; Sastry, M. *J. Colloid Interface Sci.* **2004**, *269*, 126.
(26) Shen, P.; Lee, W. H. *Nano Lett.* **2001**, *1*, 12, 707.

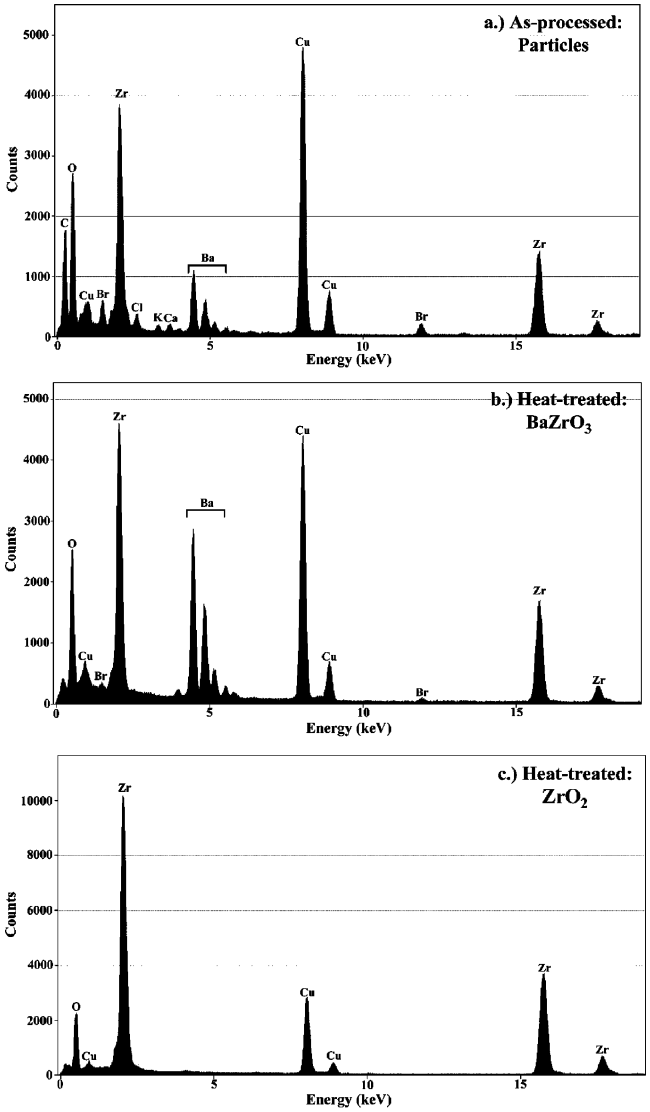

Figure 3. EDS spectra of (a) as-processed nanoparticles, (b) $BaZrO_3$, and (c) ZrO_2 particles from the postheat-treated samples.

curvature to them of varying degrees. While XRD identified these particles as $Ba(OH)_2(H_2O)_3$, interaction with the electron beam of the microscope transformed these particles to the BaO_2 structure. The rods appeared to be composed of multiple grains or subgrains of the barium hydroxide phase,

Table 1. Measured Interplanar Spacing (*d*) from the Selected Area Diffraction Pattern in Figure 4b Is Compared with Values for $BaZrO_3$ and ZrO_2 from Powder Diffraction File Numbers 6-0399 and 88-1007, Respectively

ring	$d_{measured}$ (Å)	$BaZrO_3$ (cubic) (*hkl*); *d* (Å)	ZrO_2 (tetragonal) (*hkl*); *d* (Å)
1	2.999	(110); 2.964	(101); 2.950
2	2.543		(110); 2.545
3	2.113	(200); 2.096	
4	1.798	(211); 1.712	(112); 1.810
5	1.492	(220); 1.482	
6	1.534		(103); 1.549

which upon exposure to the electron beam developed into a segmented particle consisting of smaller grains of BaO_2 linked together by a twinned interface. A high-resolution image of a twinned interface within one of the converted BaO_2 particles is shown in Figure 2d. Twinning of the interface was determined to be on the {112} planes of the tetragonal BaO_2. The fast Fourier transformation (FFT) of the lattice image clearly illustrates this twinning.

An increase in particle size was observed for the crystalline, 700 °C heat-treated samples over that of the amorphous as-deposited material. A typical TEM image of the particles is shown in Figure 4a. Sintering or attachment points between the particles were not observed with the particles consisting of single crystals. None of the rodlike $Ba(OH)_2(H_2O)_3$ particles were observed following heat-treatment. Through electron diffraction, it was revealed that the particles were a mixture of two different crystallographic phases. Examination of the ring-pattern, Figure 4b, revealed that all the intensities observed could not be associated with the $BaZrO_3$ phase alone. The ring pattern was checked against different mixed Ba−Zr−O species. The tetragonal ZrO_2 phase was found to account for the additional reflections observed within the ring pattern (Table 1), while also sharing an overlap with some of the $BaZrO_3$ intensities, confirming what was observed through XRD.

The mean particle diameter of the heat-treated sample containing both $BaZrO_3$ and ZrO_2 phases was determined to be 17.3 nm and is shown statistically in Figure 5. This was determined from several bright-field TEM images of particle agglomerations, providing a total of 150 individually measured particles. To differentiate the chemical makeup of the particles and provide some statistics as to the size and

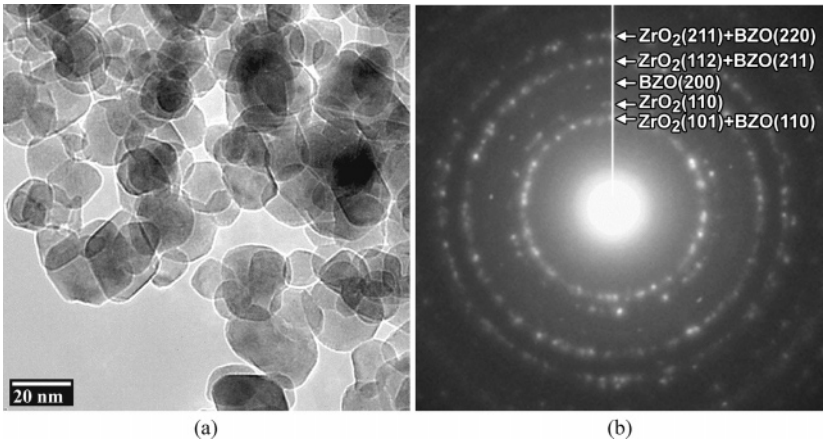

Figure 4. TEM micrographs of nanoparticles following heat treatment at 700 °C for 0.5 h in air. (a) Low magnification image illustrating the size distribution of particles with (b) selected area diffraction pattern showing a mixture of $BaZrO_3$ and ZrO_2 phases.

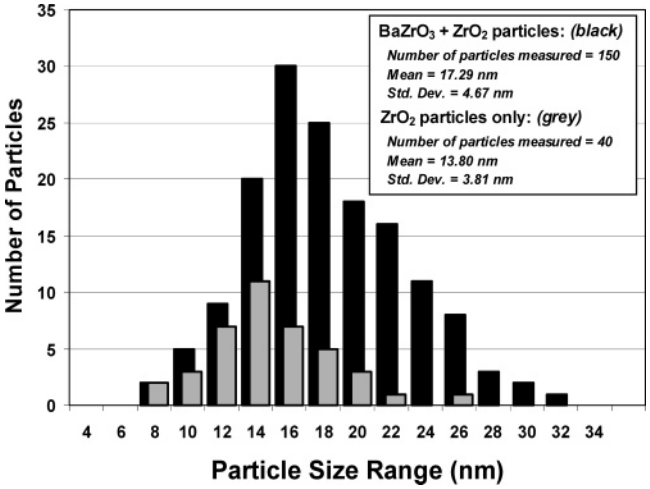

Figure 5. Size distributions of the nanoparticles after a 700 °C, 0.5 h exposure in air. Shown are separate histograms for measured diameters of $BaZrO_3$ plus ZrO_2 particles from bright-field TEM images and of ZrO_2 particles measured independently from dark-field images.

quantity of ZrO_2, a series of bright- and dark-field images were taken of several different particle agglomerations. Each of the dark-field images used a selected {110} diffracting plane of the ZrO_2 particles identified within the ring-like SAD pattern of the particle agglomeration (similar to that of Figure 4b). The particle size distribution of 40 individually measured ZrO_2 particles from this method is also shown in Figure 5. The average ZrO_2 particle size was determined to be 13.8 nm with the distribution slightly shifted to smaller particle sizes than that of the combined $BaZrO_3$ and ZrO_2 data. Although this was useful in providing data on the particle size distribution of ZrO_2, a rough estimate as to the number of ZrO_2 to $BaZrO_3$ particles was approximately 1 to 25. The quantity of ZrO_2 to $BaZrO_3$ should not be taken directly from the histograms shown in Figure 5, as they are only representations of the particle size distributions. Because only a select number of {110} ZrO_2 planes could be utilized in a given series of dark-field images, confidence in the quantity of ZrO_2 particles within a given agglomeration is low. While accurate determination of the chemical composition of individual particles had to be done through EDS, differentiating the two phases could be done on a first approximation through the particle morphology.

An example of one of the larger particles identified as $BaZrO_3$ is shown in Figure 6a oriented with its [110] direction normal to the image or in parallel with the electron beam. The EDS spectrum from this particle is shown in Figure 3b. The insert within the high-resolution image of the particle in Figure 6a is a FFT taken from a region within the $BaZrO_3$ particle not overlapped with its neighbors.

A smaller particle determined to be ZrO_2, Figure 7a, is shown oriented with its [010] direction parallel to the beam. The EDS spectrum taken from this particle is shown in Figure 3c. It should be noted that a small quantity of Br was detected in the composition of the $BaZrO_3$ particle but not within the ZrO_2 particle. The HREM lattice images of the $BaZrO_3$ and ZrO_2 particles at first appear to be similar, although well-defined differences are clearly illustrated within the FFT taken from each image and are translated into the general shape of the particles.

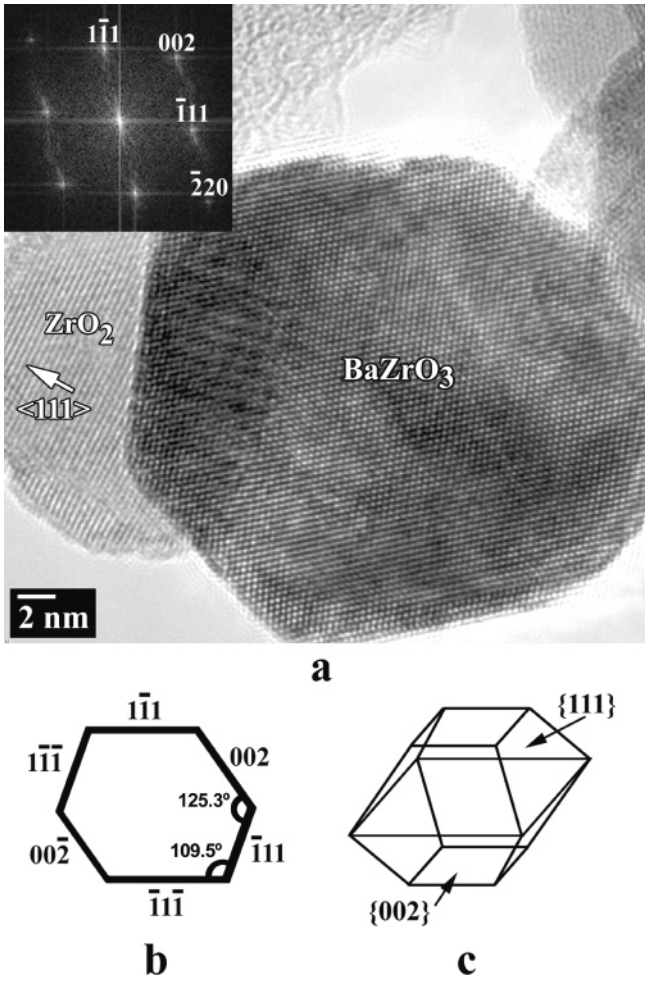

Figure 6. (a) HREM image of a $BaZrO_3$ particle with insert showing the fast Fourier transformation of the lattice image. Schematic illustrations of (b) the [110] projection of the $BaZrO_3$ particle observed in the HREM image and (c) the three-dimensional particle shape characterized as a truncated octahedral with eight {111} and two {002} surfaces.

Both the $BaZrO_3$ and ZrO_2 particles have a faceted morphology and consist of defect-free single crystals. The $BaZrO_3$ particles can be described as a truncated octahedron with {111} faces and {002} truncated surfaces, whereas the image and FFT of the ZrO_2 particle matches that of a decahedron.[27] The $BaZrO_3$ particle has the same shape and surface features that have been commonly observed for nanoparticles of CeO_2.[28−30] The faceted surfaces reported on for CeO_2 are clear experimental evidence as to the earlier modeling predictions by Sayle et al.[31,32] and Conesa.[33] These predictions suggested that the {111} planes are the most energetically favorable for termination in the CeO_2 structure followed by {110} and {211}, while the {100} planes are

(27) José-Yacamán, M.; Ascencio, J. A. Electron Microscopy Study of Nanostructured and Ancient Materials. In *Handbook of Nanostructured Materials and Nanotechnology*; Nalwa, H. S., Ed.; Academic Press: San Diego, CA, 2000; Vol. 2.
(28) Zhang, F.; Jin, Q.; Chan, S.-W. *J. Appl. Phys.* **2004**, *95*, 8, 4319.
(29) Wu, L.; Wiesmann, H. J.; Moodenbaugh, A. R.; Klie, R. F.; Zhu, Y.; Welch, D. O.; Suenaga, M. *Phys. Rev. B* **2004**, *69*, 125415.
(30) Sathyamurthy, S.; Leonard, K. J.; Debastani, R. T.; Paranthaman, M. P. *Nanotechnology* **2005**, submitted.
(31) Sayle, T. X. T.; Parker, S. C.; Catlow, C. R. A. *Surf. Sci.* **1994**, *316*, 329.
(32) Sayle, D. C.; Sayle, T. X. T.; Parker, S. C.; Catlow, C. R. A.; Harding, J. H. *Phys. Rev. B* **1994**, *50*, 19, 14498.
(33) Conesa, J. *Surf. Sci*. **1995**, *339*, 337.

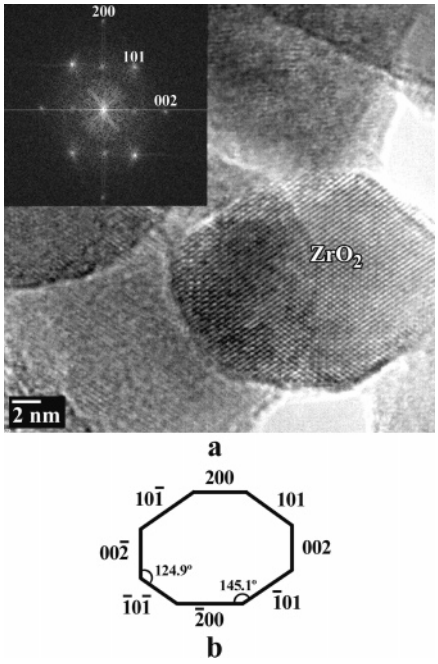

Figure 7. (a) HREM image of a ZrO_2 particle aligned with its [010] parallel to the beam, with insert showing the fast Fourier transformation of the nonoverlapping portion of the lattice image. (b) Schematic illustrations of the [010] projection of the ZrO_2 particle shown in the HREM image.

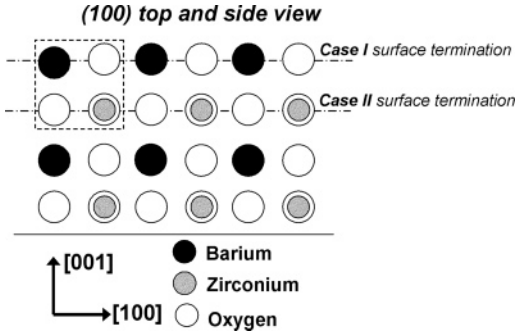

Figure 8. Top and side view of the (100) surface of the $BaZrO_3$ perovskite structure. Termination of the (100) surface may either be on the BaO or ZrO_2 nonpolar layers. The repeating unit is shown outlined by the dashed box.

energetically unstable due to a net dipole moment normal to the surface. However, removal of 50% of the atoms from the outermost O^{2-} layer allows for the {100} surface to maintain a zero net dipole moment.

The appearance of the {111} and {100} surfaces in the perovskite structured $BaZrO_3$ has led us to briefly review the stability of these surfaces due to the important interest in $BaZrO_3$ nanoparticles in areas of electronics, fuel cells, and as substrate materials. The surface terminations in the perovskite structure are a little more complicated than that of the fluorite structure of CeO_2. Illustrations of the (100), (110), and (111) surfaces viewed from both the top and tangentially as if perfectly cleaved are shown in Figures 8−10, respectively. The (100) surface (Figure 8) is an example of a type I surface that consists of layers that are charge neutral and have no net dipole moment in their repeating unit.[34] Therefore, the (100) surface can either be a BaO-terminated surface or a ZrO_2-terminated surface. While

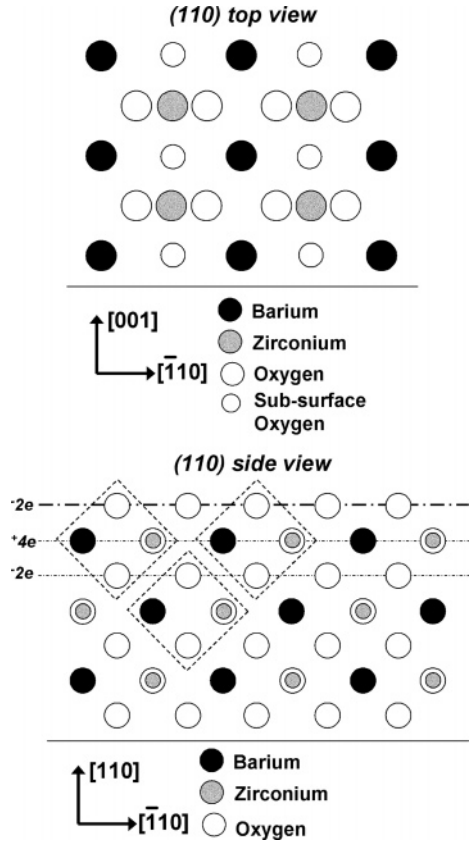

Figure 9. Top and side schematic view of the ideally cleaved (110) oxygen terminated surface of $BaZrO_3$. Side view reveals charged polar layers of O_2 and BaZrO producing an infinite dipole moment perpendicular to the surface unless 50% of the surface oxygen atoms are removed, resulting in a stoichiometrically correct zero dipole moment surface.

the exact termination is not known for $BaZrO_3$, experimental evidence and theoretical calculations suggest that surface terminations incorporating the tetravalent species are typical for the $BaTiO_3$ and $SrTiO_3$ perovskites,[35−39] even though Ti can have a valence of +3 or +2. The (100) surface has the lowest energy, requiring no further modification to the charges at its surface or in stoichiometry to maintain a nonpolar surface.

This is not the case for the (110) surface, which consists of charged planes (O_2−BaZrO−O_2−BaZrO−) arranged symmetrically (Figure 9).[40] If the O_2 terminated (110) surface is ideally cleaved (as shown in Figure 9), it would have an infinite dipole moment perpendicular to the surface and therefore be unstable. Through removal of every other oxygen atom at the surface, the structure maintains a surface with charged planes but a zero net dipole moment in its repeating unit characteristic of a type-II surface. The removal of the oxygen from the top surface layer maintains a chemical stoichiometry through the material as delineated by the dashed lines in Figure 9. Atomistic structure calculations of

(34) Noguera, C. *J. Phys.: Condens. Matter* **2000**, *12*, R367.
(35) Padilla, J.; Vanderbilt, D. *Phys. Rev. B* **1997**, *56*, 3, 1625.
(36) Heifets, E.; Eglitis, R. I.; Kotomin, E. A.; Maier, J.; Borstel, G. *Surf. Sci.* **2002**, *513*, 211.
(37) Cord, B.; Courths, R. *Surf. Sci.***1985**, *162*, 34.
(38) Hikita, T.; Hanada, T.; Kudo, M.; Kawai, M. *J. Vac. Sci. Technol., A* **1993**, *11*, 2649.
(39) Hikita, T.; Hanada, T.; Kudo, M.; Kawai, M. *Surf. Sci.* **1993**, *287*−*288*, 377.
(40) Heifets, E.; Evarestov, R. A.; Kotomin, E. A.; Dorfman, S.; Maier, J. *Sensors Actuators, B* **2004**, *100*, 81.

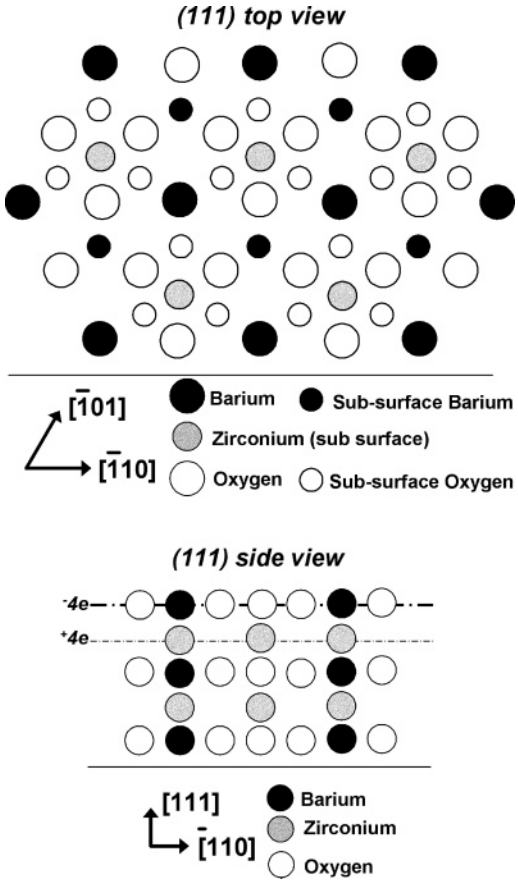

Figure 10. Top and side schematic views of the ideally cleaved (111) BaO_3^{4-} terminated surface of the $BaZrO_3$ crystal. The surface construction consists of layers of charged layers alternating between BaO_3^{4-} and Zr^{4+}.

the polar (110) surfaces in perovskite crystals have been studied considerably, in both the asymmetric configuration shown in Figure 9 and for similar oxygen terminated and metal terminated configurations.[40−42] While the configuration presented in Figure 9 has one of the lowest calculated energies, the removal of half of the oxygen atoms would disturb the balance of interatomic forces along the surface and is possibly the reason it was not observed experimentally in this study. Although (110) surfaces have been experimentally produced in $SrTiO_3$ following ultrahigh vacuum annealing, they consisted of reconstructed step ledge surfaces rather than a planar (1 × 1) surface structure.[43,44] The reconstructed step ledges may accommodate the varying valance charge of the Ti atoms in $SrTiO_3$ at the expense of increased surface energy. However, the more stable Zr^{4+} in $BaZrO_3$ may make this improbable.

The (111) surface consists of alternating polar layers of BaO_3^{4-} and Zr^{4+} and is shown in Figure 10 in both top and side views.[45] Limited experimental and theoretical work is available on the structure of the (111) surface in perovskites, with most work centered on $SrTiO_3$. Earlier experimental studies on $SrTiO_3$ have shown that stable (1 × 1) structures on (111) are possible when prepared by Ar bombardment and subsequent annealing at 600 K.[46−48] Later work showed that the unreconstructed surface was stable up to 1373 K with the top terminated layer consisting of either SrO_{3-x} or Ti, with the Ti terminated layer possessing a 3-fold symmetry associated with the Ti^{2+} species.[48] Similarly, scanning tunneling microscopy observations on $BaTiO_3$ showed that the (1 × 1) (111) surface was producible in Ar bombarded samples annealed at 1470 K in oxygen, although distinction as to BaO_3^{4-} or Ti^{4+} termination could not be made.[48] While these provide examples of planar (111) surfaces, different preparation conditions for $SrTiO_3$ were reported to yield reconstructed Ti-rich faces showing terraces and steps,[50] suggesting that the surface structure is sensitive to preparation conditions. A theoretical investigation of the electronic and atomic structures of the $SrTiO_3$ (110) and (111) (1 × 1) surfaces using a total-energy, semiempirical Hartree−Fock method has been performed for various surface termination stoichiometry.[51,52] In this work, the stability of the various (110) and (111) surface terminations was examined in terms of surface energy. It was determined that for the (111) surfaces, the surface energy was relatively independent of surface composition and was marginally higher than that for the (110) surfaces, although still close to that of the nonpolar (100) surface.

The appearance of the (111) surface on the $BaZrO_3$ nanoparticles in this investigation offers further experimental evidence for the stability of this surface in perovskite materials. In the particles that were observed through TEM, no evidence of a step-ledge or reconstructed surfaces was observed for the (100) and (111) surfaces. Further work on evaluating these surfaces and examining possible termination structures is currently being investigated. As proposed for $SrTiO_3$,[51] a strong electron redistribution in the (111) surface and subsurface layers may be substantial enough to overcome the macroscopic dipole moment created by the polar orientation. The effect of additional impurities to $BaZrO_3$, as in the detectable level of Br from EDS analysis, may also play an important role in the stabilization of the polar (111) surfaces. Although it is not known whether Br is fully incorporated into the structure or exists as a film covering the particles, due to it not being detected with the ZrO_2 particles suggests the former.

The use of reverse micelle synthesis has been shown to be successful in the processing of $BaZrO_3$ nanoparticles. However, the presence of the ZrO_2 phase indicates a compositional instability, possibly associated with the solubility of the $Ba(OH)_2$ phase in alkaline conditions. In work on sol-precipitation synthesis of $BaZrO_3$, it has been reported that the first solid to nucleate was zirconium hydroxide,[7,8] with nonstoichiometric $BaZrO_3$ particles (Ba/Zr < 1) devel-

(41) Kotomin, E. A.; Heifets, E.; Dorfman, S.; Fuks, D.; Gordon, A.; Maier, J. *Surf. Sci*. **2004**, *566−568*, 231.
(42) Kotomin, E. A.; Heifets, E.; Maier, J.; Goddard, W. A., III *Phys. Chem. Chem. Phys*. **2003**, *5*, 4180.
(43) Brunen, J.; Zegenhagen, J. *Surf. Sci*. **1997**, *389*, 349.
(44) Bando, H.; Aiura, Y.; Haruyama, Y.; Shimizu, T.; Nishihara, Y. *J. Vac. Sci. Technol., B* **1995**, *13*, 3, 1150.
(45) Asthagiri, A.; Niederberger, C.; Francis, A. J.; Porter, L. M.; Salvador, P. A.; Sholl, D. S. *Surf. Sci*. **2003**, *537*, 134.
(46) Lo, W. J.; Somorjai, G. A. *Phys. Rev. B* **1977**, *17*, 4942.
(47) Ferreer, S.; Somorjai, G. A. *Surf. Sci*. **1980**, *94*, 41.
(48) Tanaka, H.; Kawai, T. *Surf. Sci*. **1996**, *365*, 437.
(49) Hagendorf, Ch.; Schindler, K.-M.; Doege, T.; Neddermeyer, H. *Surf. Sci*. **1998**, *402−404*, 581.
(50) Sigmund, W. M.; Rotov, M.; Jiang, Q. D.; Brunen, J.; Zegenhagen, J.; Aldinger, F. *Appl. Phys. A* **1997**, *64*, 219.
(51) Pojani, A.; Finocchi, F.; Noguera, C. *Appl. Surf. Sci*. **1999**, *142*, 177.
(52) Pojani, A.; Finocchi, F.; Noguera, C. *Surf. Sci*. **1999**, *442*, 179.

oping after aging for short periods of time or at lower temperatures.[8] The use of Ba-rich starting solutions to compensate for this depletion is also under investigation.

Conclusions

Nanoparticles of the perovskite structured $BaZrO_3$ were prepared through reverse micelle synthesis, a novel and cost-effective approach to produce nanoscaled materials. The as-processed powder was a mixture of amorphous Ba−Zr−O and crystalline $Zr_{0.95}O_2$ particles with an average diameter of approximately 7.5 nm. Heat treatment of the powders to 700 °C in air for 0.5 h was sufficient to convert the material to crystalline $BaZrO_3$, although a minor quantity of ZrO_2 particles was still present. Average particle size of the heat-treated powder was increased to 17.3 nm. Both crystalline $BaZrO_3$ and ZrO_2 particles exhibited a faceted morphology, with the shape of the $BaZrO_3$ particles exhibiting {100} and polar {111} surface terminations. In addition to observing the relatively stable {100} truncation, the appearance of the {111} surfaces instead of {110} suggests a lower surface energy and more stable surface configuration for {111}.

Acknowledgment. This work was sponsored by the U.S. Department of Energy, Office of Basic Energy Sciences−Division of Materials Sciences, Office of Electric Transmission and Distribution−Superconductivity program. This work was performed at Oak Ridge National Laboratory, managed by UT-Battelle, LLC for the U.S. DOE under Contract DE-AC05-00OR22725. The authors thank Steven J. Zinkle for his support along with Naoyuki Hashimoto and Fred A. List, III for their discussions.

CM0506454